Substrate surface engineering for high-quality silicon/aluminum superconducting resonators

C T Earnest[1,2], J H Béjanin[1,2], T G McConkey[1,3], E A Peters[1,2], A Korinek[4],
H Yuan[4] and M Mariantoni[1,2]

[1] Institute for Quantum Computing, University of Waterloo, 200 University Avenue West, Waterloo,
Ontario N2L 3G1, Canada
[2] Department of Physics and Astronomy, University of Waterloo, 200 University Avenue West, Waterloo,
Ontario N2L 3G1, Canada
[3] Department of Electrical and Computer Engineering, University of Waterloo, 200 University Avenue
West, Waterloo, Ontario N2L 3G1, Canada
[4] Canadian Centre for Electron Microscopy, Department of Materials Science and Engineering, McMaster
University, 1280 Main Street West, Hamilton, Ontario L8S 4M1, Canada

E-mail: matteo.mariantoni@uwaterloo.ca

Abstract
Quantum bits (qubits) with long coherence times are an important element for the implementation
of medium- and large-scale quantum computers. In the case of superconducting planar qubits,
understanding and improving qubits' quality can be achieved by studying superconducting planar
resonators. In this paper, we fabricate and characterize coplanar waveguide resonators made from
aluminum thin films deposited on silicon substrates. We perform three different substrate surface
treatments prior to aluminum deposition: one chemical treatment based on a hydrofluoric acid clean;
one physical treatment consisting of a thermal annealing at 880 °C in high vacuum; and one
combined treatment comprising both the chemical and the physical treatments. The aim of these
treatments is to remove the two-level state (TLS) defects hosted by the native oxides residing at the
various samples' interfaces. We first characterize the fabricated samples through cross-sectional
tunneling electron microscopy, acquiring electron energy loss spectroscopy maps of the samples'
cross sections. These measurements show that both the chemical and the physical treatments almost
entirely remove native silicon oxide from the substrate surface and that their combination results in
the cleanest interface. Additionally, we analyze the effects of the various substrate treatments on
the roughness of the silicon surface by means of atomic force microscopy surface morphology
mapping. We then study the quality of the resonators by means of microwave measurements in
the 'quantum regime', i.e., at a temperature $T \sim 10\,\mathrm{mK}$ and at a mean microwave photon
number $\langle n_{\mathrm{ph}} \rangle \sim 1$. In this regime, we find that both surface treatments independently improve
the resonator's intrinsic quality factor by $\approx 172\%$. The highest quality factor is obtained for the
combined treatment, $Q_{\mathrm{i}} \approx 0.82$ million, corresponding to an improvement by $\approx 256\%$. Finally, we
find that the TLS quality factor averaged over a time period of 3 h is ~ 3 million at $\langle n_{\mathrm{ph}} \rangle \sim 10$,
indicating that substrate surface engineering can potentially reduce the TLS loss below other losses
such as quasiparticle loss and flux noise.

Keywords: quantum computing, superconducting planar resonators, silicon substrate engineering,
hydrofluoric acid dip, thermal annealing, transmission electron microscopy, loss tangent

(Some figures may appear in colour only in the online journal)

1. Introduction

Quantum computers capable of outperforming the most advanced classical computers are closer to reality than ever before [1]. Quantum processors comprising a mere 50 or 100 physical quantum bits (qubits) have the potential to show a significant computational advantage over classical supercomputers [2]. Among the many physical systems used to implement qubits [3], superconducting circuits [4, 5] remain one of the most promising candidates to realize medium- and, possibly, large-scale quantum computers [6]. The past five years have witnessed a steady increase in the size of superconducting quantum computers [7–10] as well as a continuous increase in qubit lifetime [11–13] and decrease in computational error rates [14–16].

Scaling up superconducting quantum computers while maintaining low error rates [17] requires even more accurate qubit control and measurement methods as well as longer qubit lifetimes. Superconducting qubits are made from superconducting thin films (typically aluminum (Al) or niobium) deposited and patterned above dielectric substrates (typically silicon (Si) or sapphire). Thus, the two main dissipation phenomena for this type of qubits are associated with quasiparticle loss in the metal [18] and dielectric loss [13]. The latter, in particular, is due to native oxide regions that reside at the various qubit interfaces, which are the substrate–metal (SM) and the substrate–air (vacuum) (SA) interfaces, as well as the less critical metal–air (vacuum) (MA) interface [13, 19–21]. Research has shown that these oxide films host so-called two-level state (TLS) defects [22–24], which act as a distribution of 'unwanted qubits' interfering with the actual qubit computational states [25, 26].

A simple approach to study TLS loss in superconducting devices is realized by fabricating coplanar waveguide (CPW) resonators and measuring their microwave properties at low temperature, $T \sim 10\,\mathrm{mK}$, and low excitation power or low mean microwave photon number, $\langle n_{\mathrm{ph}} \rangle \sim 1$ [27], i.e., at qubit operating conditions. In fact, CPW resonators are characterized by lossy native oxide regions also residing at the SM, SA, and MA interfaces. A fundamental characteristic of such resonators is the intrinsic (or internal) quality factor Q_{i}, which allows us to extrapolate the dielectric loss tangent $\tan \delta$ [28, 29]. These measurements make it possible to characterize and improve the device's fabrication process and, thus, to mitigate TLS loss. Additionally, superconducting CPW resonators can be used to investigate and reduce quasiparticle loss [30]. The ultimate aim of all these studies is to produce superconducting planar resonators with the highest possible Q_{i} at $T \sim 10\,\mathrm{mK}$ and $\langle n_{\mathrm{ph}} \rangle \sim 1$. While this may not directly translate to correspondingly long-lived qubits (due to the higher complexity of qubit design and fabrication [31]), it provides a reasonable estimate of the qubit energy relaxation time $T_{\mathrm{r}} = Q_{\mathrm{i}}/(2\pi f_{\mathrm{q}})$, where f_{q} is the qubit transition frequency [31]. In addition, implementing very long-lived planar resonators may make it possible to further scale superconducting quantum computing

architectures based on so-called 'cat codes' [32], which rely heavily on high-quality resonators.

A variety of methods have been shown to reduce TLS loss such as thoughtful material choices [33–35], attention to device geometry and size [13, 34], and fabrication process improvements [19, 31, 36–38]. Recently, experimental studies have focused on Al films (due to its long-term stability and the self-limiting nature of native Al oxide) and Si substrates (due to the ease of fabrication and compatibility with classical integrated circuit technology) [13, 31, 38, 39]. At this point in time, the Si/Al planar distributed resonators with the highest quality are those characterized in [31], with $Q_{\mathrm{i}} \approx 2.5$ million at low temperature and low mean photon number. The effects of substrate engineering have been well studied and reported for Al films on sapphire substrates [12, 36]; fewer aspects have been investigated in the case of Si/Al resonators [19, 31, 38].

In this paper, we present a detailed study of substrate surface engineering methods based both on chemical and on physical cleaning treatments. We show the effects of each method on the TLS loss of Si/Al superconducting CPW resonators, using the methods separately and in combination. The compared methods are an *ex situ* 'RCA' Standard Clean-1 (or RCA SC-1) process [40] immediately followed by hydrofluoric (HF) acid etching (or HF dip) [19], and two different *in situ* thermal annealing treatments in a high-vacuum (HV) environment [41]. We focus on Al films deposited by way of electron-beam evaporation instead of molecular beam epitaxy (MBE), using the same system we also use to fabricate superconducting qubits; the physical cleaning treatments are carried out in this system.

We first characterize the various methods by means of cross-sectional transmission electron microscope (TEM) measurements of the SM interface by acquiring electron energy loss spectroscopy (EELS) maps. In addition, we characterize the surface morphology of the SA interface with atomic force microscopy (AFM). We then perform microwave measurements of superconducting CPW resonators and use them to obtain Q_{i} at low temperature, both at a high and at a low mean photon number. Additionally, we measure the time fluctuations of the total TLS loss $F \tan \delta_{\mathrm{TLS}}$, where F is the CPW filling factor [28], over the course of 3 h long measurements. The resonators fabricated with either the chemical or the physical surface treatment show an improvement over unprocessed devices; a combination of the two treatments results in the biggest improvement with $Q_{\mathrm{i}} \approx 0.82$ million at $T \sim 10\,\mathrm{mK}$ and $\langle n_{\mathrm{ph}} \rangle \sim 1$ and a time average $\langle F \tan \delta_{\mathrm{TLS}} \rangle \sim 3.5 \times 10^{-7}$ or, equivalently, an average TLS quality factor $\langle Q_{\mathrm{TLS}} \rangle \sim 3$ million at $T \sim 10\,\mathrm{mK}$ and $\langle n_{\mathrm{ph}} \rangle \sim 10$. The overall improvement associated with the combined surface treatment corresponds to $\approx 256\%$.

Aside from characterizing the effects of each individual surface treatment, we demonstrate that a standard electron-beam evaporation system with *in situ* annealing capabilities allows us to reach similar or higher resonator quality compared to an MBE system [38].

This paper is organized as follows. In section 2, we describe the surface engineering methods used to fabricate the samples studied in this work (see section 2.1), the microwave measurement setup (see section 2.2), and the TEM and EELS as well as AFM techniques used to perform thin film metrology (see section 2.3). In section 3, we show the thin film metrology (see section 3.1) as well as the intrinsic quality factor measurements, including time fluctuation analysis and sample aging effects (see section 3.2). In section 4, we compare our findings to those presented in previous studies (see section 4.1), discuss the behavior of our resonators at high mean photon number (see section 4.2), compare the effects of an 880 °C anneal to those of a 950 °C anneal for a short and a long annealing time of 10 and 60 min, respectively (see section 4.3), and provide a detailed analysis on the filling factors associated with our resonator design compared to that in [31] (see section 4.4). Finally, in section 5, we summarize our results and outline a procedure that may reduce TLS loss below all other loss mechanisms in planar devices. We also describe the effects that our substrate surface treatments will likely have when combined with qubit fabrication processes. Additionally, in appendix A, we provide details on the resonator measurement and fitting procedures and, in appendix B, details on the numerical simulations used in section 4.4.

2. Methods

The aim of this section is to provide the details required to perform and reproduce the substrate surface engineering methods presented in this paper. We show the sample and resonator layouts and describe the setup used for the microwave measurements. Finally, we specify the steps followed to prepare the samples for the TEM and EELS characterization as well as for the AFM study.

2.1. Substrate surface engineering: methods

Six samples are fabricated in order to study the effects of various substrate surface engineering methods: one control sample with no substrate surface treatment ('Unprocessed'); one sample prepared with a chemical cleaning treatment that comprises an RCA SC-1 process and an HF dip ('RCA 1 + HF'); one sample prepared with a physical treatment consisting of a short thermal annealing step at 880 °C for 10 min ('880 °C Anneal'); one sample prepared with both the chemical cleaning treatment and the short thermal annealing step at 880 °C for 10 min ('RCA 1 + HF + 880 °C Anneal'). Additionally, one sample is prepared with a short thermal annealing step at 950 °C for 10 min ('950 °C Anneal, 10 min') and one with a long thermal annealing step also at 950 °C, but for 60 min ('950 °C Anneal, 60 min'). These treatments are all applied to the substrate directly before the deposition of the Al thin film.

All the samples for this study are fabricated on high-resistivity (>10 kΩ cm) 500 μm thick 4 inch float-zone undoped Si (100) wafers. The details of the surface engineering methods are:

(1) *RCA 1 + HF*—a 10 min RCA SC-1 process (a bath of $NH_4OH:H_2O_2:H_2O$, 1:1:5, at 75 °C), immediately followed by a 1 min bath in buffered oxide etchant containing 1% HF acid. After cleaning, the wafers are dried with nitrogen (N) gas and placed immediately (within ~10 min) in the load-lock of the deposition system;

(2) *880 °C Anneal*—a 30 min ramp to 880 °C, followed by a 10 min anneal at 880 °C in HV at a pressure $\lesssim 4 \times 10^{-7}$ mbar;

(3) *950 °C Anneal*—a 30 min ramp to 950 °C, followed by a 10 or 60 min anneal at 950 °C in HV at a pressure $\lesssim 4 \times 10^{-7}$ mbar. This is the highest temperature attainable in our system.

At the end of each annealing process, the sample is allowed to cool overnight in the same chamber down to a temperature of ≈24 °C before *in situ* Al deposition. During the cooldown period, the chamber reaches ultra-high vacuum (UHV) with a pressure ~1 × 10^{-10} mbar. The Unprocessed sample is a brand-new wafer that is not submitted to any chemical or physical treatment prior to Al deposition.

The annealing temperatures are measured by means of a type K thermocouple in the heating element, which is calibrated to the temperature of the wafer during commissioning via a thermocouple attached to the front side of the wafer (the heating element heats from the back side). We estimate that the actual temperature of the wafer can fluctuate by ~±15 °C; this uncertainty is obtained from a set of tests with a thermocouple on the front of a molybdenum plate. We notice that the center of a 4 inch wafer is more homogeneously heated than the wafer edges; thus, we characterize dies only from the wafer center.

The Al films are deposited by means of an UHV electron-beam physical vapor-deposition (EBPVD) system from Plassys-Bestek SAS, model MEB 550 SL3-UHV. Each film is 100 nm thick and is deposited at a rate of 2 Å s^{-1} from a 99.999% pure Al shot with a large pellet size to reduce the surface-to-volume ratio. The base pressure in the EBPVD chamber is ~10^{-10} mbar before evaporation and ~2.0 × 10^{-8} mbar during evaporation.

Each sample is patterned by means of optical lithography using a 1 μm thick layer of Microposit S1811 positive photoresist from the Shipley Company-MicroChem Corp. The photoresist is developed in Microposit MF-319 developer also from Shipley and then etched using an inductively coupled plasma (ICP) etcher from Oxford Instruments plc, model Plasmalab System 100 ICP380 III–V and metals chlorine etcher. Each sample is immediately transferred into a water bath after etching to remove any remaining chlorinated species on the sample surface and kept soaked in water for at
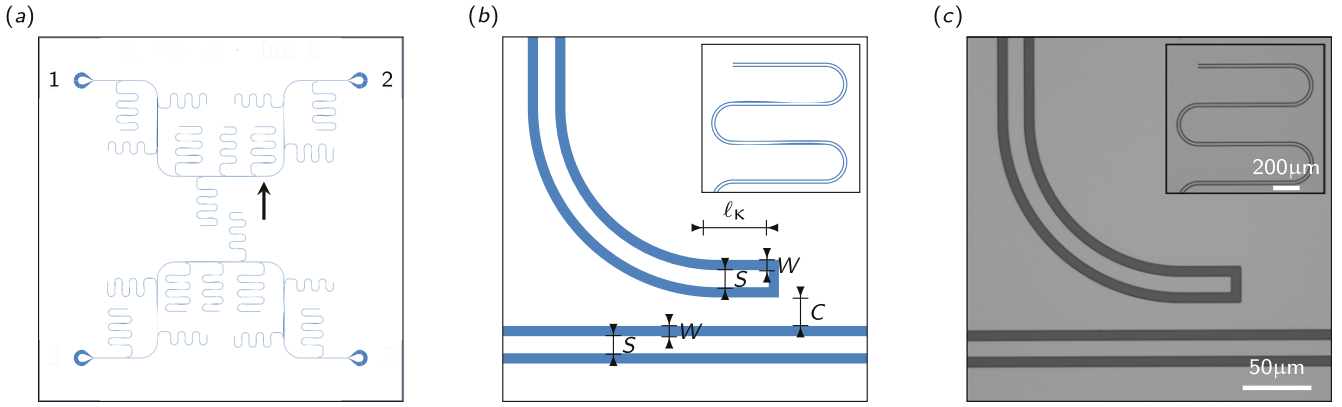
Figure 1. Sample and resonator layouts. (a) Two feed CPW transmission lines are capacitively coupled to two sets of ten meandered quarter-wave resonators. The only measured feed line is the one where the input and output ports are labeled 1 and 2, respectively. The transmission line configuration is similar to our sample layouts in [42]. The black arrow indicates the resonator with $\tilde{f}_0 = 4.5$ GHz. (b) Geometrical details and characteristic dimensions of the resonator with $\tilde{f}_0 = 4.5$ GHz. *C*: coupling-strength distance between the feed line and resonator; ℓ_κ: coupling-strength length between the feed line and resonator (see main text for details); *S*: center conductor width of CPW feed line and resonator; *W*: gap widths of CPW feed line and resonator. Inset: ending region of the meandered resonator showing how the resonator centered conductor is shorted to ground, resulting in a quarter-wave resonator. (c) Optical microscopy image of the resonator details in (b), as fabricated.

least 10 min. The remaining photoresist is removed in two different consecutive 7 min baths of Remover PG, a proprietary n-methyl-2-pyrrolidinone-based stripper from the MicroChem Corp., placed in an ultrasonic bath heated to 70 °C. Residual Remover PG is removed in an unheated bath of isopropyl alcohol, which is itself removed with N gas. An additional double layer of photoresist is applied as a protection before dicing and removed after dicing with the same stripping procedure as above.

Figure 1 shows the sample and resonator layouts. The overall sample layout is depicted in figure 1(a), which shows two feed CPW transmission lines capacitively coupled to ten meandered quarter-wave resonators each with a different designed resonance frequency $\tilde{f}_0$, in a multiplexed design (see the works in [42, 43] for similar designs from our research group). The only measured feed line is the one where the input and output ports are labeled 1 and 2, respectively. We measure the feed-line transmission coefficient S_{21} in the frequency range between 4–8 GHz and, for consistency, select one resonator from each sample with the same designed $\tilde{f}_0 = 4.5$ GHz, as indicated in figure 1(a).

Figure 1(b) shows the geometrical details and characteristic dimensions of the resonator with $\tilde{f}_0 = 4.5$ GHz. The resonator is capacitively coupled to the corresponding feed line with a designed coupling strength $\kappa = 40$ kHz. This coupling strength is determined by the distance $C = 37$ μm between the feed line and the resonator as well as by the length $\ell_\kappa = 88$ μm for which the resonator and transmission line run parallel to each other. The feed line and resonator feature a center conductor of width $S = 15$ μm and gaps of width $W = 9$ μm. Figure 1(c) shows an optical microscopy image of the resonator details in (b), as fabricated.

2.2. Resonator measurements: methods

The diced samples are mounted in a quantum socket package analogous to that described in [42] and anchored to

the mixing chamber of a dilution refrigerator with base temperature $T \sim 10$ mK. The measurement setup, which features heavily attenuated microwave lines as well as careful infrared and magnetic shielding, is described in detail in [42]. The total attenuation of the input microwave channel that connects the room-temperature electronics to the samples is $\sim$76 dB at 5 GHz. All measurements are performed by means of a vector network analyzer (VNA) from Keysight Technologies Inc., model PNA-L N5230A.

2.3. Thin film metrology: methods

The material effects of each substrate surface treatment in correspondence of the SM interface are studied through cross-sectional TEM measurements (see figure 2). Cross sections of the samples are prepared within two different types of focused ion beam (FIB) systems; one system from Carl Zeiss AG, model NVision 40 and a brand-new system from Thermo Fisher Scientific, model Helios G4 plasma FIB (or pFIB). The NVision 40 FIB system works on traditional gallium+ (Ga+) ions to mill the samples, whereas the pFIB system works on xenon+ (Xe+) ions. Xe+ ions do not react with the oxygen (O) content of the samples and, thus, do not induce additional sample contamination [44]. In fact, we use Ga+ ions only for the RCA 1 + HF and RCA 1 + HF + 880 °C Anneal samples, where the O content is small. The Unprocessed and 880 °C Anneal samples are first milled with Ga+ ions; after noticing considerable contamination, we milled new samples using Xe+ ions with the newly acquired pFIB system. The other two samples show very small Ga+ ion implantation and, thus, are not milled using the pFIB system.

After depositing a mixture of carbon and platinum (Pt) on the sample's surface to prevent damage, the FIB systems are used to prepare thin sample's sections. Then, two trenches are milled on both sides of the area of interest using either a Ga+ or Xe+ ion beam. The resulting thin section is lifted out from the sample using a micromanipulator needle. The
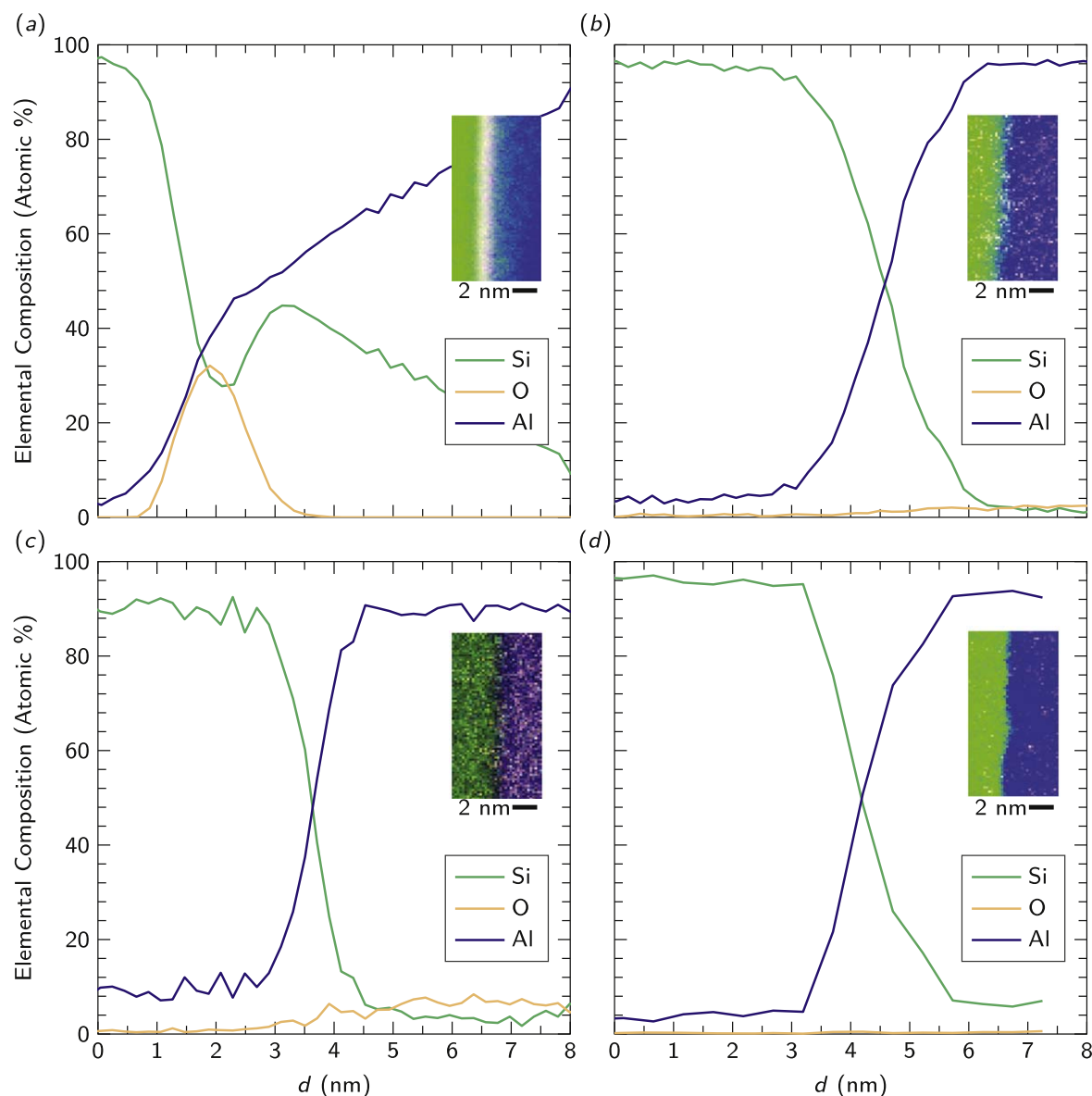
Figure 2. Elemental composition as atomic percentage versus depth d for Si, O, and Al at the SM interface of each of the main four samples. Data is collected with EELS over a rectangular area (inset) and averaged to give the atomic percentage shown in the line graph (see main text for details). Si: green (medium gray); O: light orange (light gray); Al: blue (dark gray). (a) Unprocessed sample (pFIB). (b) RCA 1 + HF sample (Ga+ FIB). (c) 880 °C Anneal sample (pFIB). (d) RCA 1 + HF + 880 °C Anneal sample (Ga + FIB).

cross section is subsequently attached to a copper TEM grid using Pt. Finally, the cross section is thinned to electron transparency, ∼80 nm thickness, followed by a low-voltage cleaning at 5 kV for the Ga+ ion beam and 2 kV for the Xe+ ion beam.

The cross sections are imaged in a TEM system from the FEI Company, model Titan 80–300, operated at 200 kV. The system is equipped with a CEOS image and probe corrector and a Gatan imaging filter from Gatan, Inc. (type 'Quantum Energy Filter'). Low magnification scanning TEM images are acquired to assess the overall quality of the sample and the roughness of the Si/Al interface. High-angle annular dark-field high-resolution scanning TEM micrographs are acquired to visualize the interface between the Si substrate and the Al film.

EELS maps are acquired to investigate the formation of an oxide layer at the Si/Al interface. The maps are acquired with a step size of 2 Å; the dwell time per spectrum is set to 0.01 s, with a detector binning of [1, 130] and 1 eV per channel. The convergence semi-angle of the electron beam is set to 19.1 mrad and the collection semi-angle to 55 mrad. The beam current is set to ≈150 pA in order to avoid beam induced sample damage.

EELS elemental quantification is calculated using the Gatan digital micrograph 3.22 software[5]. The spectra are aligned to eliminate energy shifts during acquisition. For the background fit of the edges a power law model is fitted to

---

[5] See http://gatan.com/products/tem-analysis/gatan-microscopy-suite-software for details on the Gatan Microscopy Suite software.
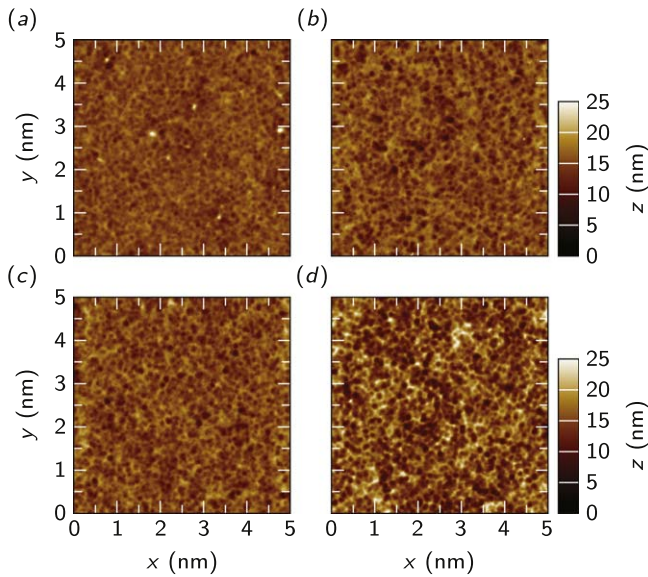
Figure 3. Surface morphology mapping of the SA interface of each of the main four samples. Data is taken with AFM scans (see main text for details). Each scan is performed on the *xy*-plane, with colorbar scales indicating the height *z*. For each sample, all scans are repeated in two different regions of the SA interface. Only one of the two scans is shown; similar results are obtained in the second scan. (a) Unprocessed sample. (b) RCA 1 + HF sample. (c) 880 °C Anneal sample. (d) RCA 1 + HF + 880 °C Anneal sample. A quantitative analysis of these data is summarized in table 1.

the spectra. The Hartree-Slater cross-section model is used for quantification. The energy loss near edge structure region of the peaks is excluded up to 40 eV.

The material effects of each substrate surface treatment in correspondence of the SA interface are studied through AFM surface morphology mapping (see figure 3 and table 1). The surface texture is assessed with nanoscale resolution by means of a system from the Bruker Corporation, model Digital Instruments NanoScope IIIa AFM Controller with MultiMode scanning probe microscopy capabilities. The AFM scans are taken using a tapping imaging mode with tapping amplitude of 2 V, scanning rate of 1 Hz, scanning size of 5 μm (i.e. a scanning area of 5 μm × 5 μm), 512 samples, in data imaging mode 'height' with a data scale of 25 nm; the tip used is a 160 μm Si cantilever with a nominal resonance frequency of 300 kHz and a radius of 9 nm.

3. Results

In this section, we study the effects and show the efficacy of the various substrate surface engineering methods by presenting both thin film metrology and microwave measurements. In particular, we study quality factors as a function of mean photon number, quality factor time fluctuations, and sample aging.

3.1. Thin film metrology: results

Figure 2 shows the elemental composition as atomic percentage for Si, O, and Al at the SM interface of each sample, as measured

Table 1. Quantitative analysis of surface roughness at the SA interface of each of four samples prepared with different substrate surface treatments. R_a: average surface roughness; R_q: rms surface roughness. All values are obtained by analyzing the AFM data in figure 3 (see main text for details).

| Sample	R_a (nm)	R_q (nm)
Unprocessed	1.09	1.41
RCA 1 + HF	1.52	1.93
880 °C Anneal	1.50	1.90
RCA 1 + HF + 880 °C Anneal	2.16	2.69

with EELS. As expected, these measurements demonstrate that the RCA 1 + HF chemical cleaning treatment is effective at removing almost entirely the Si native oxide and that this oxide does not reform in the time between cleaning and placement into the Al deposition system. In addition, the measurements show that the 880 °C Anneal also removes almost entirely the Si native oxide present on the substrate. When applied separately, both the chemical and physical cleaning treatments result in noticeable O implantation in the Al region when compared to the Unprocessed sample. The combined treatment, instead, not only cleans the interface from any oxide, but also leads to a very sharp transition between the Si and Al regions, without any noticeable O interdiffusion or implantation in either of these two regions.

Additionally, we notice that the RCA 1 + HF and 880 °C Anneal samples appear to show a very small amount of O implantation in the Si region when compared to the Unprocessed sample. As noted in section 2.3, in the case of the RCA 1 + HF sample, which is prepared with a Ga+ FIB, O implantation is likely due to FIB contamination. As for the 880 °C Anneal sample, the average O implantation level in Si is close to the noise floor of our EELS measurement. Thus, we expect negligible effects due to O implantation in Si on the resonators' quality. In section 4, we compare these results with those obtained for the 950 °C Anneal, 10 and 60 min samples.

Figure 3 shows the surface texture at the SA interface of each sample, as measured with AFM. We perform a quantitative analysis to find the average as well as rms surface roughness, R_a and R_q, respectively. The results are reported in table 1 and indicate a clear increase in substrate surface roughness with an increase in complexity of the surface treatment. The Unprocessed sample is the smoothest and the RCA 1 + HF + 880 °C Anneal sample the roughest. Interestingly, the RCA 1 + HF and 880 °C Anneal samples show a comparable roughness, further confirming the effect of these two separate treatments on the SA interface to be similar, as in the case of the SM interface. Additionally, it is worth noting that the change in R_q is moderate, ranging from a minimum of 1.41 to a maximum of 2.69 nm (see section 4.2 for more details on the effects of surface roughness and a comparison with other studies).

3.2. Resonator measurements: results

As explained in sections 2.1 and 2.2, we measure the transmission coefficient S_{21} of feed line 1–2 in figure 1(a) in the frequency range between 4–8 GHz and, for consistency, select
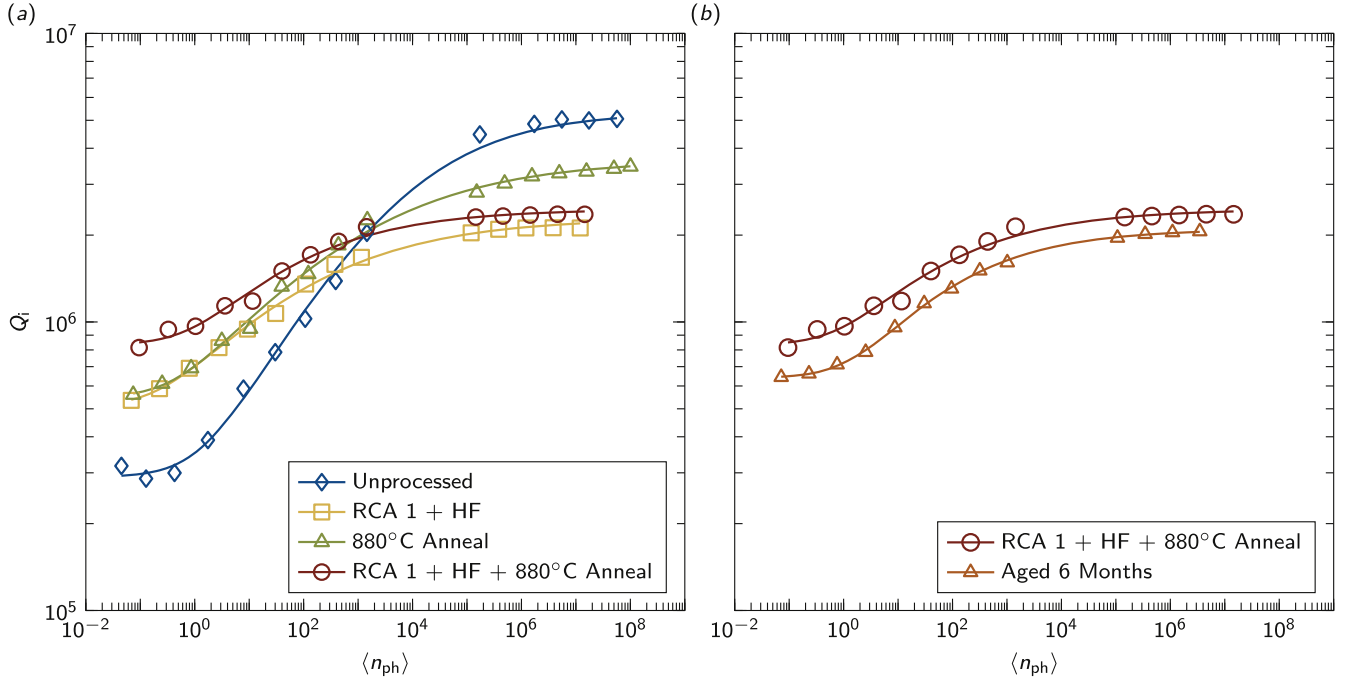
Figure 4. Resonator S-curve measurements. Symbols correspond to data and solid lines to fitting curves obtained using the modified photon-dependent TLS model of (1). All measurements are performed at $T \sim 10$ mK (see main text for details). (a) Intrinsic quality factor Q_{i} versus mean photon number $\langle n_{\mathrm{ph}} \rangle$ for one resonator on each of the four samples: Unprocessed, RCA 1 + HF, 880 °C Anneal, and RCA 1 + HF + 880 °C Anneal. (b) The data for the resonator on sample RCA 1 + HF + 880 °C Anneal in (a) are compared to those for a resonator fabricated on a similar sample, but aged over a time period of 6 months.

Table 2. Quantitative analysis of loss mechanisms for one resonator on each of four samples prepared with different substrate surface treatments. f_0: Fitted resonance frequency; Q_{c}^*: fitted rescaled coupling quality factor; Q_{LP}: fitted internal quality factor at the lowest measured mean photon number; $\langle n_{\mathrm{ph}} \rangle^{\mathrm{c}}$: critical mean photon number (see main text for details); α: deviation from the standard TLS model; $F \tan \delta_{\mathrm{TLS}}^0$: total TLS loss at zero photon number and zero temperature fitted from (1); $F \tan \delta_{\mathrm{TLS}}$: approximate total TLS loss estimated as in (2); $1/Q^*$: non-TLS loss fitted from (1); $1/Q_{\mathrm{HP}}$: approximate non-TLS loss.

Sample	f_0 (GHz)	Q_{c}^* 10^6	Q_{LP} 10^6	$\langle n_{\mathrm{ph}} \rangle^{\mathrm{c}}$ —	α —	$F \tan \delta_{\mathrm{TLS}}^0$ 10^{-6}	$F \tan \delta_{\mathrm{TLS}}$ 10^{-6}	$1/Q^*$ 10^{-6}	$1/Q_{\mathrm{HP}}$ 10^{-6}
Unprocessed	4.487	0.39	0.32	1.17	0.33	3.27	2.93	0.19	0.20
RCA 1 + HF	4.501	0.27	0.53	0.21	0.25	1.53	1.42	0.44	0.47
880 °C Anneal	4.512	0.34	0.56	0.40	0.24	1.56	1.50	0.27	0.29
RCA 1 + HF + 880 °C Anneal	4.506	0.34	0.82	0.78	0.28	0.80	0.80	0.41	0.42

one resonator from each sample with the same designed $\tilde{f}_0 = 4.5$ GHz and $\kappa = 40$ kHz. The resonator transmission measurements are fitted as described in appendix A to give the actual resonance frequency f_0, rescaled coupling quality factor Q_{c}^* [36], and internal quality factor Q_{i} at the highest and lowest measured mean photon number, Q_{HP} and Q_{LP}, respectively (see table 2). The mean photon number $\langle n_{\mathrm{ph}} \rangle$ is estimated from the input excitation power (see appendix A.2). All measurements are performed at $T \sim 10$ mK.
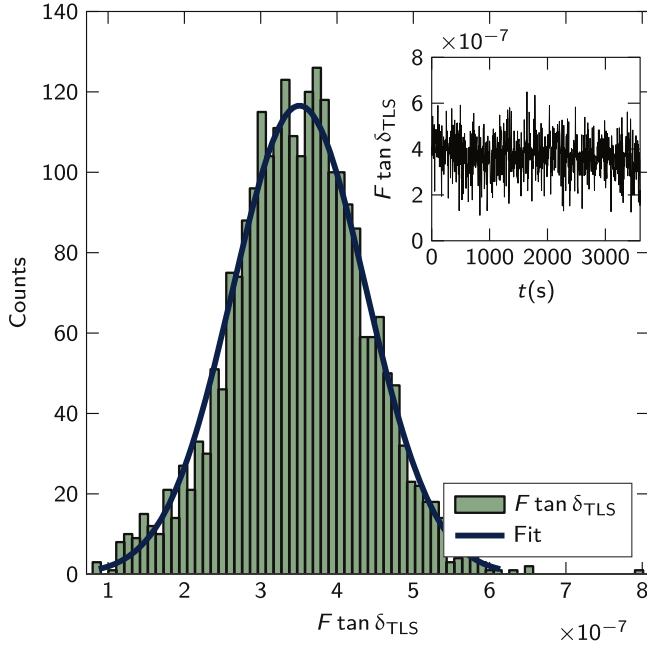
Figure 4(a) shows Q_{i} as a function of $\langle n_{\mathrm{ph}} \rangle$, with characteristic S-curve shape [29], for four resonators on samples fabricated using different substrate surface treatments. As expected, the highest Q_{LP} is found for the resonator on the RCA 1 + HF + 880 °C Anneal sample, $Q_{\mathrm{LP}} \approx 0.82 \times 10^6$. Notably, the resonators on the RCA 1 + HF and the 880 °C

Anneal samples have both $Q_{\mathrm{LP}} \approx 0.55 \times 10^6$, indicating that the separate chemical and physical substrate surface treatments lead to similar improvements compared to the resonator on the Unprocessed sample, which has $Q_{\mathrm{LP}} \approx 0.32 \times 10^6$.

Despite an increase in SA surface roughness with surface treatment (see table 1), each individual treatment as well as the combined treatment still result in a higher Q_{LP}. This indicates that the benefits of our substrate surface treatments at the SM interface outweigh the increased roughness at all interfaces.

In order to obtain a more accurate estimate of the resonator TLS loss, we invert the data of each S-curve and fit it to the modified photon-dependent TLS model [38, 39]

$$\frac{1}{Q_{\mathrm{i}}(\langle n_{\mathrm{ph}} \rangle)} \cong F \tan \delta_{\mathrm{TLS}}^0 \left(1 + \frac{\langle n_{\mathrm{ph}} \rangle}{\langle n_{\mathrm{ph}} \rangle^{\mathrm{c}}} \right)^{-\alpha} + \frac{1}{Q^*}, \quad (1)$$

Figure 5. Time fluctuations of TLS loss. TLS loss $F \tan \delta_{\mathrm{TLS}}$ versus time t plotted as a histogram comprising 70 bins. The measurement is performed over a time period of 3 h (see main text for details). The solid line is a fit to a normal distribution. Inset: Time trace associated with the histogram, showing $F \tan \delta_{\mathrm{TLS}}$ versus t up to $t = 3600$ s.

where $F \tan \delta_{\mathrm{TLS}}^0$ is the total TLS loss at zero photon number and zero temperature, $\langle n_{\mathrm{ph}} \rangle^c$ is a critical mean photon number above which the TLS defects start to be saturated, α is an exponent indicating the deviation from the standard TLS model (in the standard model $\alpha = 1/2$), and the constant offset $1/Q^*$ accounts for all other (non-TLS) losses ($1/Q^* \sim 1/Q_{\mathrm{HP}}$). The fitting curves are overlaid to the data in figure 4. The fitted values of $\langle n_{\mathrm{ph}} \rangle^c$, α, $F \tan \delta_{\mathrm{TLS}}^0$, and $1/Q^*$, as well as [21]

$$F \tan \delta_{\mathrm{TLS}} \cong \frac{1}{Q_{\mathrm{LP}}} - \frac{1}{Q_{\mathrm{HP}}} \qquad (2)$$

are reported in table 2. Figure 4(b) shows $Q_{\mathrm{i}}(\langle n_{\mathrm{ph}} \rangle)$ for one resonator on an RCA 1 + HF + 880 °C Anneal sample fabricated at the same time as previous samples, but aged over a time period of ~6 months. The sample is stored in atmosphere in a cleanroom environment prior to measurement. Aging effects on the resonator quality are very small and uniform as a function of $\langle n_{\mathrm{ph}} \rangle$.

Finally, we examine the fluctuations of the TLS loss $F \tan \delta_{\mathrm{TLS}}$ as a function of time t by repeating the same transmission measurement for the RCA 1 + HF + 880 °C Anneal sample at $\langle n_{\mathrm{ph}} \rangle \approx 10$ over a period of 3 h. Each measurement lasts ≈3 s and the measurements are carried out in succession without a predetermined timing. Each transmission measurement is fitted and $F \tan \delta_{\mathrm{TLS}}$ is found as in (2). Figure 5 shows $F \tan \delta_{\mathrm{TLS}}(t)$ as a histogram, with an inset displaying the raw time trace truncated at $t = 3600$ s. The histogram mean value (time average) is $\langle F \tan \delta_{\mathrm{TLS}} \rangle \sim 3.5 \times 10^{-7}$, with a standard deviation ~0.9×10^{-7}.

We note that the time properties of TLS defects [45] have been studied following a variety of different approaches, from resonator noise measurements [46–48] to qubit T_{r} [49] and qubit energy level [50] characterization.

4. Discussion

In this section, we compare our results to the state of the art, we study the behavior of our resonators at high mean photon number, the effects of annealing at high temperature, and compare the effects of substrate treatments with those of filling factor engineering.

4.1. Comparison to the state of the art

It is worth comparing our results with those reported in other studies. In [36], it was found that cleaning a sapphire substrate by means of activated molecular oxygen O_2^* while heating the substrate in HV at 850 °C or only heating the substrate in UHV at 850 °C has the most significant benefits on the CPW resonator quality in the quantum regime. We find similar results by chemically cleaning a Si substrate *ex situ* and then annealing it at 880 °C in HV. Additionally, our results are based on electron-beam evaporated Al instead of MBE Al. In fact, our highest Q_{LP} is slightly higher than the highest Q_{LP} obtained in [36] using electron-beam evaporation without any special clean.

Compared to the study in [19], we add a thermal annealing step to the overall cleaning process. This step increases Q_{LP} by ~50% when combined with an *ex situ* chemical clean. In [31], it is shown that by performing an HF dip clean of a Si substrate followed by annealing at 900 °C in an UHV MBE system results in a (2×1) surface reconstruction. This is a very similar surface treatment as the combined clean described in our work. The resonators fabricated on such a substrate using an Al electron-beam evaporator attached to the MBE annealing chamber have $Q_{\mathrm{LP}} \sim 2$ million, which is approximately a factor of two larger than for our best resonator. A similar result was found in [38], where, however, the Al film were grown using an MBE system and the best quality factor is slightly lower than ours. An important addition of our work is to clearly break down the cleaning process into separate steps, characterizing each step using both thin film metrology and microwave characterization.

The study in [38] characterizes Q_{i} of resonators on samples fabricated using both wet and ICP (dry) etch processes. They do not find a clear correlation between either process and the resulting Q_{i}. The work in [51] indicates that a one-step deep reactive ion etch can be used to implement suspended three-dimensional transmon qubits with longer T_{r}. Additionally, most of the studies on high-quality superconducting resonators use an ICP etch process for sample fabrication (see, e.g., [13, 21, 36]). Hence, we use an ICP etch process to ease comparison. Moreover, ICP etch processes are

compatible with Si trenching [13, 21, 37] and, thus, it is highly desirable to use them if the intention is to trench the SA interfaces in future experiments (see section 5).

4.2. Behavior at high mean photon number

It is worth noting that the quality factors at high mean photon number, Q_{HP}, shown in figure 4(a) vary significantly for the different S-curves, which, in fact, cross each other when increasing $\langle n_{ph} \rangle$. This means that while the TLS loss clearly decreases when applying suitable surface treatments, the non-TLS loss does not. In particular, we find a reasonable correlation between the surface roughness at the SA and SM interfaces (see figure 3 and table 1 as well as figure 2) and drop in Q_{HP} (see figure 4). In fact, the Unprocessed sample, which is the smoothest, displays the highest Q_{HP}. Following this argument the RCA 1 + HF + 880 °C Anneal sample should be characterized by the lowest Q_{HP}, which, instead is similar to that for sample RCA 1 + HF.

It is thus worth exploring the effect of surface roughness more in detail in order to plan a suitable approach to further investigate this issue. All substrates studied in this work undergo a surface treatment before the Al film deposition. Hence, we can assume the roughness of the Si substrate underneath the conductors of the CPW resonators (SM interfaces) to be approximately the same as for the Si gaps (SA interfaces)[6]. This conjecture can be qualitatively confirmed by inspecting the cross-sectional TEM measurements shown in figure 2, which reveal an increase in substrate and metal surface roughness at the SM interface with an increase in complexity of the surface treatment. The alternations caused inside the conductor can increase the conductor surface impedance. The increased loss factor due to the conductor surface roughness at the SM interface is obtained from the Morgan–Hammerstad–Bekkadal model [52, 53]

$$\rho \cong 1 + \frac{2}{\pi} \arctan\left[1.4\left(\frac{R_q}{\delta_s}\right)^2\right], \qquad (3)$$

where δ_s is the field penetration depth. When $R_q \gg \delta_s$, $\rho \sim 2$, which, thus, is the maximum increased loss factor. In the case of an Al superconducting thin film at a temperature T much lower than the film critical temperature T_c, $T \sim 10$ mK $\ll T_c \approx 1.2$ K, and at relatively low frequencies $f < 10$ GHz, the field penetration depth can be approximated with the London penetration depth [54, 55][7] of thin film Al at $T = 0$ K, $\delta_s \approx \lambda_L(0) \sim 100$ nm [56]. Under these assumptions the effect of the roughest SM surface in table 1 corresponds to $\rho \approx 1.001$, i.e., an increase in loss of $\approx 0.1\%$. Notably, the model of (3) provides an upper bound for ρ in the case of lossy superconductors [57]. Therefore, we expect the impact

of the SM surface roughness on Q_{HP} to be negligible. Our results confirm the findings of the study in [58], even though our values of R_q at the SM interface are approximately 10 times larger than in that study.

In classical applications (i.e., for resonators used in communication devices with $Q_{HP} \sim 1 \times 10^3$), since the surface roughness is typically much less than the microwave field wavelength, the roughness effects outside the conductors can be safely neglected [57] since Q_{HP} is highly dominated by other loss channels. In our case, because of the high values of Q_{HP} the effect of surface roughness at the SA interface may cause a measurable change in Q_{HP}, as also pointed out in [20]. The study in [19] shows significant variations of Q_{HP} with the SA surface roughness, although in that work R_q varies between 0.8 and 45 nm, which is a much wider range than ours and with the highest roughness much higher than ours (see table 1). Additionally, in [19] the overetching of the Si gaps is very inhomogeneous and the values of Q_{HP} are at least 10 times lower than ours, making a comparison difficult. Lastly, due to the very small electric field energy in the region up to ~3 nm (which is more than our highest value of R_q in table 1) above the MA interface (see table appendix B), we expect no effect due to surface roughness at that interface.

Further investigations will be required to understand the dependence of Q_{HP} on substrate surface treatment and potentially on surface roughness, which may become important when the TLS loss becomes negligible and non-TLS losses are the primary dissipation channels. Due to significant parameter variations from sample to sample and even between adjacent resonators on the same sample (as also reported in [38]), these studies will likely require the fabrication and measurement of a large number of samples, in the statistical spirit of the work in [21].

Another possible explanation for the drop in Q_{HP} with an increase in complexity of the surface treatment is the presence of unwanted magnetic fields in proximity of the samples. As explained in detail in [42], we use a meticulous shielding setup and we thoroughly characterize every component inside our dilution refrigerator for magnetism to ensure the magnetic field near the sample is virtually zero. However, the study in [59] shows that even an extremely small unwanted magnetic field on the order of a few microtesla can significantly deteriorate Q_i and, in particular, Q_{HP} without resorting to ground-plane holes as in our case. Additionally, the work in [60] indicates that cleaner films are less resilient to unwanted magnetic fields. They show that Q_{HP} decreases with film quality when the sample is cooled in a magnetic field.

When considering both O implantation and Si interdiffusion for values of d in the Al regions, figure 2 shows that the cleanest sample is the RCA 1 + HF sample. The RCA 1 + HF + 880 °C Anneal sample is slightly cleaner than the 880 °C Anneal sample since it shows less O implantation (even more so as it is prepared with Ga+ FIB instead of pFIB) and similar Si interdiffusion. The Unprocessed sample is the dirtiest with significant Si interdiffusion and abundant local O implantation at the Si–Al interface. Hence, we expect the Unprocessed sample to show the highest Q_{HP}, followed by the 880 °C Anneal sample,

---

[6] The surface roughness at the SM interfaces may be slightly higher than at the SA interfaces due to modest overetching of the Si gaps during lithography, which can thus smoothen out some of the SA surface roughness. The Si surfaces covered by metal obviously do not get etched during lithography.

[7] See also https://wmi.badw.de/teaching/Lecturenotes/AS/AS_Chapter8.pdf for details on the field penetration depth in superconductors.
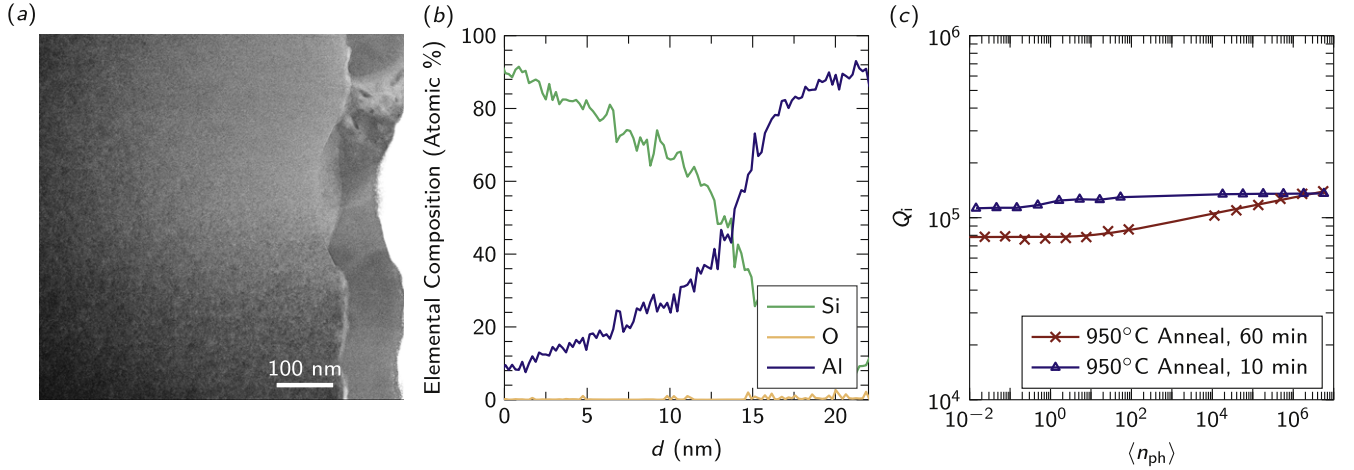
Figure 6. Effects of annealing at high temperature. (a) Cross-sectional TEM micrograph of the 950 °C Anneal, 60 min sample. (b) Atomic percentage of Si, O, and Al at the sample's SM interface. Si: green (medium gray); O: light orange (light gray); Al: blue (dark gray). Sample preparation performed using pFIB. Data is collected with EELS, as in figure 2. (c) Intrinsic quality factor Q_i versus mean photon number $\langle n_{ph} \rangle$. 950 °C Anneal, 60 min sample: crosses indicate measured data; the solid line indicates a fitting curve obtained from (1). In this case, $\alpha \sim 0.05$, indicating a large departure from the standard TLS model. 950 °C Anneal, 10 min sample: open up-pointing triangles indicate measured data; the solid line is a guide to the eye. In this case, the data does not follow the TLS model (see main text for details). Q_{LP} as well as Q_{HP} are very low for both the 10 and the 60 min sample.

the RCA 1 + HF + 880 °C Anneal sample, and, lastly, the RCA 1 + HF sample (the last two samples should have a very similar Q_{HP}). Figure 4 confirms this explanation. In fact, it may be possible that a combination of increased surface roughness at the SA interface and sample cleanness contributes to our findings for Q_{HP}.

4.3. Effects of annealing at high temperature

In addition to the 10 min anneal at 880 °C, we perform a more aggressive 950 °C anneal on one sample for 10 min and on another for 60 min. We characterize the film properties of the 950 °C Anneal, 60 min sample focusing on the SM interface by means of cross-sectional TEM measurements. As elucidated by figures 6(a) and (b), this treatment completely removes the native Si oxide at the SM interface. However, it causes significant surface roughness and damage to the crystal structure at the Si substrate surface.

As for the four main samples in figure 3, we perform an AFM surface morphology mapping of the 950 °C Anneal, 60 min sample as well, focusing on the SA interface. We find an extremely rough surface with $R_a = 14.81$ nm and $R_q = 18.36$ nm. All these effects combined together outweigh any benefit from the complete oxide removal at the SM interface, yielding a resonator with very low Q_i for all values of $\langle n_{ph} \rangle$ (see figure 6(c)). From the model in (3), we can estimate the increased loss factor due to the surface roughness at the SM interface to be $\rho \approx 1.030$, i.e., an increase in loss of $\approx 3\%$. Also in this case, the SM roughness cannot explain the drop in quality factor. However, the findings of the study in [58] confirm that a deterioration of the crystal structure at the Si substrate surface can result in much lower values of Q_i.

The 950 °C Anneal, 10 min sample yields results similar to the 60 min sample, with a low Q_i (see also figure 6(c)). It is important to observe, though, that the overall quality of the 10 min sample is superior to that of the 60 min sample. In fact, we are able to identify more dips in the S_{21} trace corresponding to the designed resonators on the sample. Additionally, the resonator at $\tilde{f}_0 = 5.5$ GHz on the 950 °C Anneal, 10 min sample is characterized by a Q_{LP} similar to the best resonator in figure 4. This result suggests that it may be possible to further optimize our substrate surface treatments by investigating in detail the annealing temperature and time (T, t)-space between the two limiting points (880 °C, 10 min) and (950 °C, 60 min).

4.4. Substrate treatments versus filling factors

Resonator and qubit dielectric losses can be mitigated by engineering the filling factor (also known as participation ratio) of the various lossy regions. In [31], for instance, the choice of larger CPW dimensions significantly reduces dielectric losses by reducing the filling factor of each lossy region. Hereafter, we refer to our CPW resonator design as design 'type 1,' with $S_1 = 15$ μm and $W_1 = 9$ μm, and to the CPW design in [31] as design 'type 2,' with $S_2 = W_2 = 24$ μm. In order to distinguish the impact of our substrate treatments versus filling factor engineering and to more accurately compare our findings to those in [31], we here perform a detailed analysis of the filling factors in designs 1 and 2.

The native oxide at any of the CPW interfaces $i = \{$SM, SA, MA$\}$ occupies a region Ω_i with volume $V_i = \ell_r \times t_i \times \ell_i$, where ℓ_r is the length of the center conductor of the CPW resonator and t_i and ℓ_i the thickness and width of Ω_i, respectively. Neglecting the native oxide regions below and above

the CPW ground planes, we can assume $\ell_{SM} = \ell_{MA} = S$ and $\ell_{SA} = W$. In general, the filling factor F_i associated with each region Ω_i is defined as the ratio between the electric energy stored in Ω_i and the total electric energy stored in the resonator, U_e [28]. It can be shown that this ratio is independent from the total charge and, thus, electric potential on the conductor. Hence, F_i has the same value at each space-time point of a standing wave on the CPW resonator [20]. Therefore, it suffices to calculate F_i as a ratio of electric energies per unit length with respect to ℓ_r,

$$F_i = \frac{\frac{\varepsilon_i}{4} \iint_{\sigma_i} dA \, \vec{E}_i \cdot \vec{E}_i^*}{\sum_j \frac{\varepsilon_j}{4} \iint_{\sigma_j} dA \, \vec{E}_j \cdot \vec{E}_j^* + \sum_i \frac{\varepsilon_i}{4} \iint_{\sigma_i} dA \, \vec{E}_i \cdot \vec{E}_i^*} \quad (4a)$$

$$= \frac{\varepsilon_i \iint_{\sigma_i} dA \, ||\vec{E}_i||^2}{4\tilde{u}_e}, \quad (4b)$$

where ε_i is the absolute electric permittivity of Ω_i, σ_i the cross-sectional surface of Ω_i on the (t_i, ℓ_i)-plane with area $A_i = t_i \times \ell_i$, dA an infinitesimal area element on the (t_i, ℓ_i)-plane, $\vec{E}_i$ the electric field within σ_i and $\vec{E}_i^*$ its complex conjugate; ε_j is the absolute electric permittivity of Ω_j with $j = \{Si, 0\}$ for the Si substrate below the CPW resonator and the vacuum region above it, respectively, σ_j the cross section of Ω_j on the same plane as σ_i, $\vec{E}_j$ the electric field within σ_j and $\vec{E}_j^*$ its complex conjugate. The sum of integrals in the denominator of $(4a)$ is the total electric energy per unit length[8] $\tilde{u}_e$ stored in the CPW resonator. The numerator in $(4b)$ is written in terms of the electric field norm squared $||\vec{E}_i||^2$. All regions Ω_i and Ω_j are assumed to be isotropic, linear, and homogeneous dielectrics.

The filling factor definition $(4b)$ can be approximated by assuming $\vec{E}_i$ to be uniform across t_i (in fact, typically $t_i \ll \ell_i$) for each region i, as in [20],

$$F_i \cong \frac{\frac{\varepsilon_i}{4} t_i \int_{\gamma_i} d\ell \, ||\vec{E}_i||^2}{4\tilde{u}_e}, \quad (5)$$

where γ_i is a line along the ℓ_i-axis with length ℓ_i.

Assuming $\varepsilon_i = 10$ and $t_i = 3 \, nm$ for each region Ω_i [20][9] for both design type 1 and design type 2, the relative filling factor of design 2 with respect to design 1 reads

$$\frac{F_{i2}}{F_{i1}} = \frac{\tilde{u}_{e1} \iint_{\sigma_{i2}} dA \, ||\vec{E}_{i2}||^2}{\tilde{u}_{e2} \iint_{\sigma_{i1}} dA \, ||\vec{E}_{i1}||^2} \quad (6a)$$

$$\cong \frac{\tilde{u}_{e1} \int_{\gamma_{i2}} d\ell \, ||\vec{E}_{i2}||^2}{\tilde{u}_{e2} \int_{\gamma_{i1}} d\ell \, ||\vec{E}_{i1}||^2}, \quad (6b)$$

where $(6a)$ and $(6b)$ are obtained from $(4b)$ and (5) for designs 1 and 2, respectively. The two resonators are assumed to have equal length ℓ_r in both designs.

___

[8] That is, the energy line density. We neglect the energy stored in the field penetration depth region.
[9] Our previous study in [29] based on x-ray photoelectron spectroscopy (XPS) measurements confirms that typical native oxide thicknesses are $\lesssim 3 \, nm$.

Table 3. Relative filling factors of design 2 with respect to design 1. Methods: exact, calculating numerically $(6a)$; approximated, calculating numerically $(6b)$. All numerical calculations are performed by means of COMSOL Multiphysics[1]. The exact absolute filling factors for all regions and both designs are reported in table A1 of appendix B. F_{i2}/F_{i1}: Relative filling factor of design 2 with respect to design 1 for $i = \{SM, SA, MA\}$ and assuming the Al film thickness to be 100 nm for both designs (see main text for details). The approximated and exact results are in excellent agreement.

Method	F_{SM2}/F_{SM1}	F_{SA2}/F_{SA1}	F_{MA2}/F_{MA1}
Exact	0.523	0.515	0.484
Approximated	0.530	0.524	0.526

___

[1] See https://comsol.com/comsol-multiphysics for details on the COMSOL Multiphysics software.

We find numerical values for both $(6a)$ and $(6b)$ by calculating the integrals numerically using the electrostatics package of the software COMSOL Multiphysics (AC/DC module) from COMSOL, Inc. The results for all regions Ω_i are reported in table 3. The approximated results found from $(6b)$ rely only on one integration step and, thus, are used as a sanity check to verify the correctness of the numerical double integrals in $(6a)$. Details about the COMSOL numerical simulations are provided in appendix B.

The results in table 3 indicate that the filling factors for design 2 (used in [31]) are all approximately one half the filling factors for design 1 (our design), $F_{i2} \sim F_{i1}/2$ for each i. Assuming $1/Q_{HP} \sim 0$ for both designs and equal loss tangents $\tan\delta_i$ for all lossy regions in both designs,

$$Q_{LP2} = \sum_i \frac{1}{F_{i2} \tan\delta_i} = 2\sum_i \frac{1}{F_{i1} \tan\delta_i} = 2 \, Q_{LP1}. \quad (7)$$

As a consequence, it should not surprise that the highest Q_{LP} in [31] is two times larger than ours for a similar substrate treatment. In absolute terms, this also shows that the high values of Q_{LP} found in this work are not significantly inflated by filling factor engineering, as they are genuinely due to low values of the loss tangents. It is worth noting, though, that we may be able to further improve the Q_{LP} of our resonators by increasing our values of S and W as in [31], with the caveat that increasing these values excessively eventually leads to radiation loss.

5. Conclusion

We show that a chemical (HF dip) or physical (thermal annealing at 880 °C in HV) treatment of a Si substrate surface positively impact the microwave performance of Al superconducting CPW resonators fabricated on such substrates. The Al films are deposited by means of electron-beam evaporation in an UHV environment, with a deposition system commonly used to fabricate superconducting qubits. No Si deep trenching is performed on any of our samples. The highest internal quality factor at low temperature ($T \sim 10 \, mK$) and low mean microwave photon number ($\langle n_{ph} \rangle \sim 1$) is obtained by performing both substrate treatments in succession, $Q_{LP} \approx 0.82$ million. This corresponds to a Q_{LP}

improvement of $\approx 256\%$ compared to the Q_{LP} of a resonator on an Unprocessed sample. Notably, the characteristic dimensions of our CPW resonators are significantly smaller than those used in, e.g., [31]; our center conductor width is $S = 15\,\mu m$ with gap widths $W = 9\,\mu m$. Thus, our design does not take significant advantage of filling factor engineering, which becomes more important for larger resonator dimensions. Aging effects on Q_{LP} are tested by measuring a resonator after storing the sample in a cleanroom environment for ~ 6 months. We find that aging has very small and uniform effects on the resonator quality.

Time fluctuations of the TLS loss for the resonator with the highest quality factor are estimated by measuring the loss over a time period of 3 h. We find a time-average TLS quality factor $\langle Q_{TLS} \rangle \sim 3$ million　at $T \sim 10\,mK$ and　$\langle n_{ph} \rangle \sim 10$, which is similar to the highest TLS quality factor measured in [21]. In that work, such a high quality factor is obtained when trenching the Si gap of the CPW line by $2.2\,\mu m$, i.e., a CPW resonator with a deep trench (see also [37] for Si deep trenching). This result suggests that by trenching our Si/Al resonators it may be possible to further enhance $\langle Q_{TLS} \rangle$ by a factor of ~ 2. This would result in $\langle Q_{TLS} \rangle \sim 6$ million, which is significantly larger than the typical internal quality factor at high mean microwave photon number of our resonators, $Q_{HP} \sim 2.5$ million. By combining deep trenching with filling factor engineering[10], we may be able to gain another factor of ~ 2, resulting in $\langle Q_{TLS} \rangle \sim 12$ million. Under these conditions, TLS defects would not be the limiting channel for dissipation, which, instead, would likely be dominated by quasiparticle loss, flux noise, vortices, metal surface roughness, and radiative loss channels.

We characterize the film properties focusing on the SM interface by means of cross-sectional TEM measurements and on the SA interface using AFM scans. These measurements show that both the HF dip chemical cleaning and thermal annealing at 880 °C almost entirely remove the native Si oxide layer at the SM interface. In both cases, we observe a small, but noticeable O implantation in the Al region and a very small O implantation in the Si region. Such implantation is absent when applying a combined chemical and physical treatment, which results in the highest Q_{LP}. In addition, we observe a clear correlation between increased substrate surface roughness and complexity of surface treatment. The increase in roughness is however moderate and does not outweigh the beneficial effects of the treatments. Furthermore, we find that a more aggressive and longer thermal anneal at 950 °C damages and roughens the substrate surface largely, negating any positive impact on the resonator quality.

We note that the absolute filling factors reported in table A1 show that the participation to loss due to the SA interface is similar to that of the SM interface, confirming previous results [13, 20, 21]. The AFM results reported in table 1 indicate a moderate increase in surface roughness at the SA interface with surface treatment. As a consequence, the surface area associated with the SA interface increases, leading to a larger volume of native Si oxide and, thus, to a higher loss that is further exacerbated by the large SA filling factor. In the

light of these findings, resorting to deep trenching of the SA interface may result in an even larger improvement of Q_{LP}.

The ultimate goal of our work is to develop and characterize substrate surface treatments that are compatible with superconducting qubit fabrication techniques. Our treatments are similar to the most complex treatment discussed in [31]. In that work, the authors clearly demonstrate that the limiting dissipation channel for qubit TLS loss is introduced by the aggressive argon ion milling step in the lift-off process used to make the qubit Josephson junctions. In the case of an Xmon transmon qubit, for example, ion milling is required to obtain a superconducting contact between the pristine Al layer used to make the qubit capacitor ('base wiring') and the junctions' leads ('electrode metal').

The authors of [31] propose and experimentally realize a method that makes it possible to mitigate the deleterious effects of ion milling. They show that CPW resonators fabricated with substrate treatments similar to ours yield $Q_{LP} \sim 2$ million. They then add ion milling sites to this high-quality resonators and show that the resulting Q_{LP} is reduced by a factor ~ 10. They show that this loss in quality can be mitigated by employing a protection process that shields the substrate from ion milling ('bandage'). When using the protection process, they are able to obtain $Q_{LP} \sim 1$ million. This value is only half of the highest Q_{LP} found in absence of ion milling sites. The missing factor of 2 may be due to flux noise [61, 62] induced by the substrate surface treatments. In fact, the study in [31] shows similar results when fabricating Xmon transmon qubits with substrate surface treatments as well as ion milling protection. Such a loss of quality, however, may still be due to only partial protection from ion milling. Hence, it will be interesting to make qubits pursuing either the method reported in [63], which introduces a cleaner ion milling process, or changing radically the junction fabrication process, as for example prescribed in [64].

Acknowledgments

---

[10] For example, by increasing S and W to $24\,\mu m$ as in [31].

Appendix A. Fits

In this appendix, we provide details on the resonator measurement and fitting procedures used to find the results presented in the main text. We use a systematic experimental routine that allows us to obtain reliable and repeatable measurements of the intrinsic quality factor of resonators, Q_i, as a function of the excitation power. This power corresponds to an equivalent mean microwave photon number, $\langle n_{ph} \rangle$. Our routine is initialized with the approximate resonance frequency f_0 and frequency span $\Delta f = f - f_0$ of the resonator to be measured; from these initial values, the routine automatically finds proper measurement ranges and normalization traces, as well as the number of traces to be averaged in order to obtain a fitting uncertainty below a certain threshold. The power is then decreased and the measurement repeated with updated parameters until the minimum desired power level is reached.

We now explain the routine in more detail. We separate the resonator measurement procedure from the resonator fitting procedure, since they are independent.

A.1. Resonator fitting procedure

The resonator fitting procedure takes as inputs transmission-coefficient (scattering parameter (or S-parameter)) S_{21} data. Figure A1 shows the magnitude of the measured transmission coefficient $|S_{21}|$ as a function of frequency f for the feed line 1–2 for each of the four samples in figure 4(a) in the frequency range between 4 and 7 GHz; the measurements are actually performed up to 8 GHz, although no resonator is designed to be above 7 GHz as confirmed by the measurements (the frequency range between 7 and 8 GHz is thus not shown). After the resonator to be investigated is selected (i.e., the resonator with designed $\tilde{f}_0 = 4.5$ GHz), the S_{21} data is taken over two narrower frequency ranges: one used for normalization; another used for resonator fitting. The *normalization data* is measured away from resonance, in the flat transmission regions on the left and right side of the resonance dip. Figure A2 shows the two spots where the normalization data is taken for the transmission-coefficient magnitude $|S_{21}|$, including a fitting line that connects them. The *resonator data* is measured close to resonance, within the resonance dip (see figure A2). We use the following fitting function [36]:

$$\tilde{S}_{21}^{-1} = 1 + \frac{Q_i}{Q_c^*} e^{i\phi} \frac{f_0}{f_0 + i2Q_i \Delta f}, \qquad (A.1)$$

where Q_c^* is the rescaled coupling quality factor of the resonator, ϕ is an offset angle, and $i^2 = -1$.

As initial fitting parameters we use $Q_i = 10^6$, $Q_c^* = 3 \times 10^5$, and $\phi = 0$. Additionally, we choose f_0 to be the frequency where $|S_{21}|$ reaches a minimum.

The resonator fitting procedure comprises the following steps:

(1) take the S_{21} normalization and resonator data as input data, as shown in figure A3;
(2) fit the normalization data in magnitude and phase separately to a line, as shown also in figure A3;
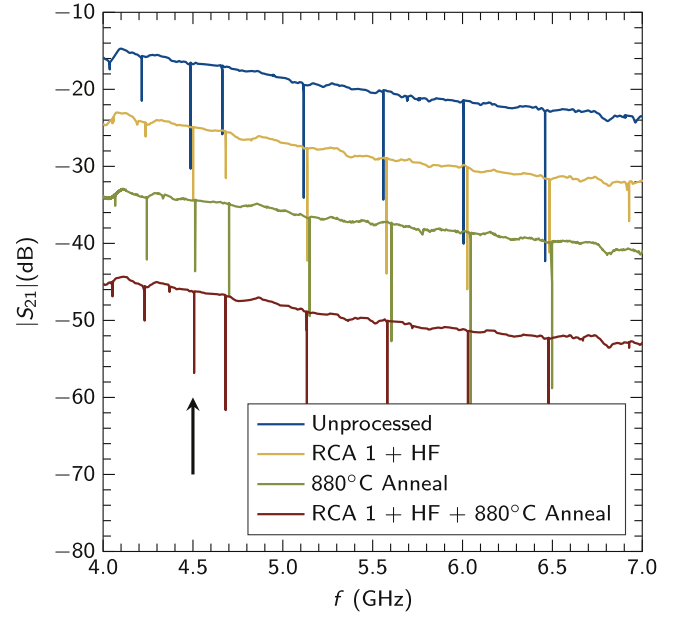
Figure A1. Transmission-coefficient measurements (see main and appendix text for details). Transmission-coefficient magnitude $|S_{21}|$ versus frequency f for each of the four samples: Unprocessed, RCA 1 + HF, 880 °C Anneal, and RCA 1 + HF + 880 °C Anneal. All measurements are performed at $T \sim 10$ mK and high $\langle n_{ph} \rangle$ using a VNA at room temperature with similar measurement parameters as in [42]. The traces are offset vertically to ease visualization, as they would otherwise almost coincide since we use the same measurement setup in all measurements. The black arrow indicates the transmission dips associated with the resonator with $f_0 \approx 4.5$ GHz for each sample.
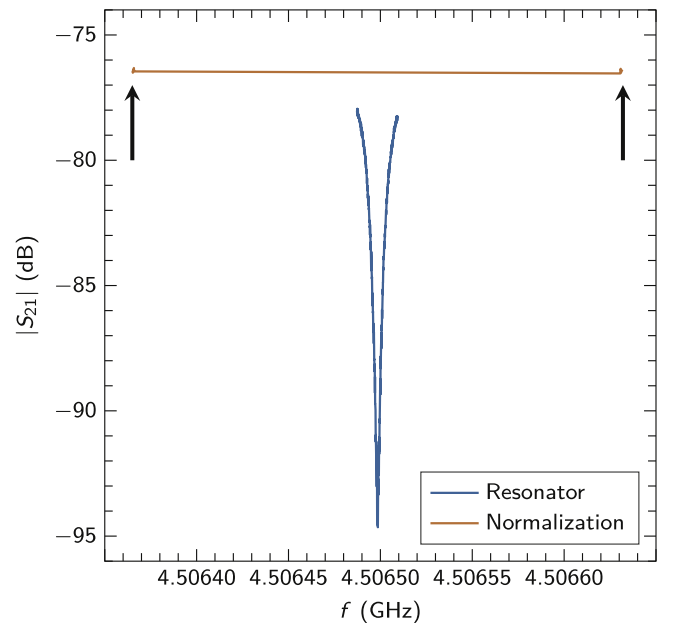
Figure A2. Normalization and resonator data. Transmission-coefficient magnitude $|S_{21}|$ versus frequency f. The resonator data is localized in proximity of f_0 ('Resonator'; blue (dark gray)). The normalization data is a set of eight data points in two regions indicated by arrows. These two regions are fitted with a line ('Normalization'; orange (light gray)).
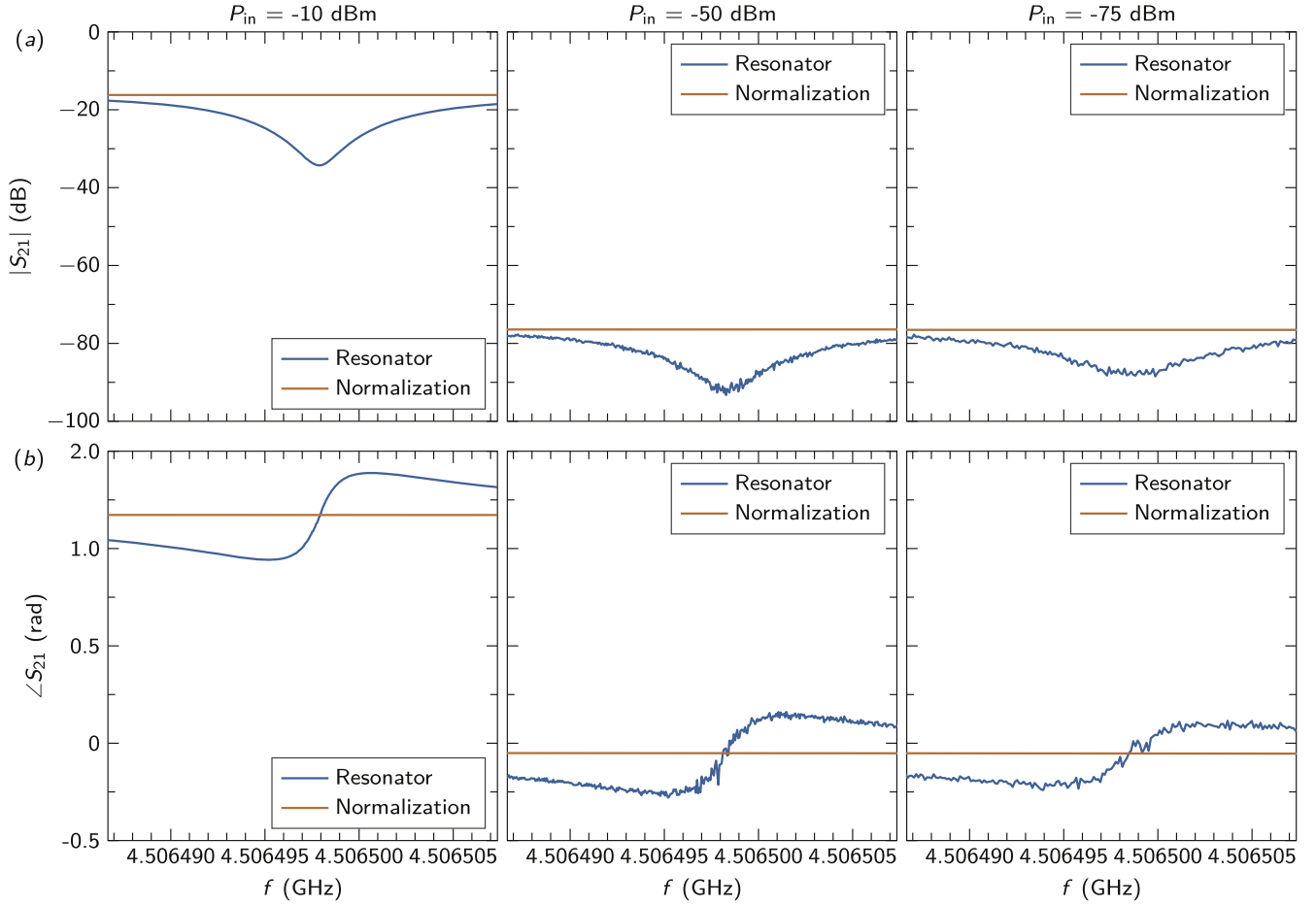
Figure A3. Resonator measurement procedure. Each panel comprises three columns, one for each different excitation power (see appendix text for details). (a) Transmission-coefficient magnitude $|S_{21}|$ versus frequency f; resonator data ('Resonator'; blue (dark gray)) and normalization line ('Normalization'; orange (light gray)). (b) Same as in (a), but for the transmission-coefficient phase $\angle S_{21}$ versus f. In both panels, the normalization lines originate from a set of eight data points in two regions far on the left and right of resonance (see figure A2).

(3) extrapolate the value of the magnitude and phase in the frequency range of the resonator data;

(4) subtract the extrapolated data from the resonator data in the complex plane. This has the effect of de-embedding the measurement setup from the data. The magnitude and phase of the normalized resonator data is shown in figure A4;

(5) invert the normalized resonator data;

(6) fit the inverted normalized resonator data to (A.1) using standard nonlinear least squares techniques, starting from a reasonable initial parameters choice;

(7) calculate the fitting errors from the covariance matrix;

(8) obtain the fitting parameters and associated errors.

A.2. Resonator measurement procedure

The resonator measurement procedure takes as inputs an approximate f_0 and $\Delta f = f - f_0$, as well as a list of VNA excitation powers $\{P_{in}^j\}$ (where $j = 1, 2, \ldots, N$ and N is an integer number) and intermediate frequency (IF) bandwidths $\{\Delta f_{IF}^j\}$. The procedure acquires a sufficient number of traces at each excitation power to satisfy a preset fitting error threshold. In our measurements, the upper bound for this threshold (Q_i error) is set

to 1%. The threshold, the number of points to measure for the resonator data and relative frequency span, and the maximum number of measured traces N_{tr} are configurable, although they are usually not changed from experiment to experiment. Typically, we measure one single trace at the highest excitation power and ~ 30 traces at the lowest powers.

The value of $\langle n_{ph} \rangle$ is estimated from the room-temperature power at the input channel, P_{in}, and the knowledge of the total input-channel attenuation coefficient α_{att}. A total attenuation of $\sim 76\,\mathrm{dB}$ corresponds to $\alpha_{att} \approx 3.98 \times 10^7$. Following [42], we find

$$\langle n_{ph} \rangle = \frac{2}{h\pi^2} \frac{Q_\ell^2}{Q_c^*} \frac{P'_{in}}{\tilde{f}_0^2}, \qquad (A.2)$$

where h is the Planck constant,

$$\frac{1}{Q_\ell} = \frac{1}{Q_i} + \frac{1}{Q_c^*} \qquad (A.3)$$

is the inverse loaded quality factor of the resonator, and $P'_{in} = P_{in}/\alpha_{att}$ is the power at the resonator input. In our estimate, we use $\alpha_{att} \approx 3.98 \times 10^7$ also for the dilution refrigerator at operating conditions.
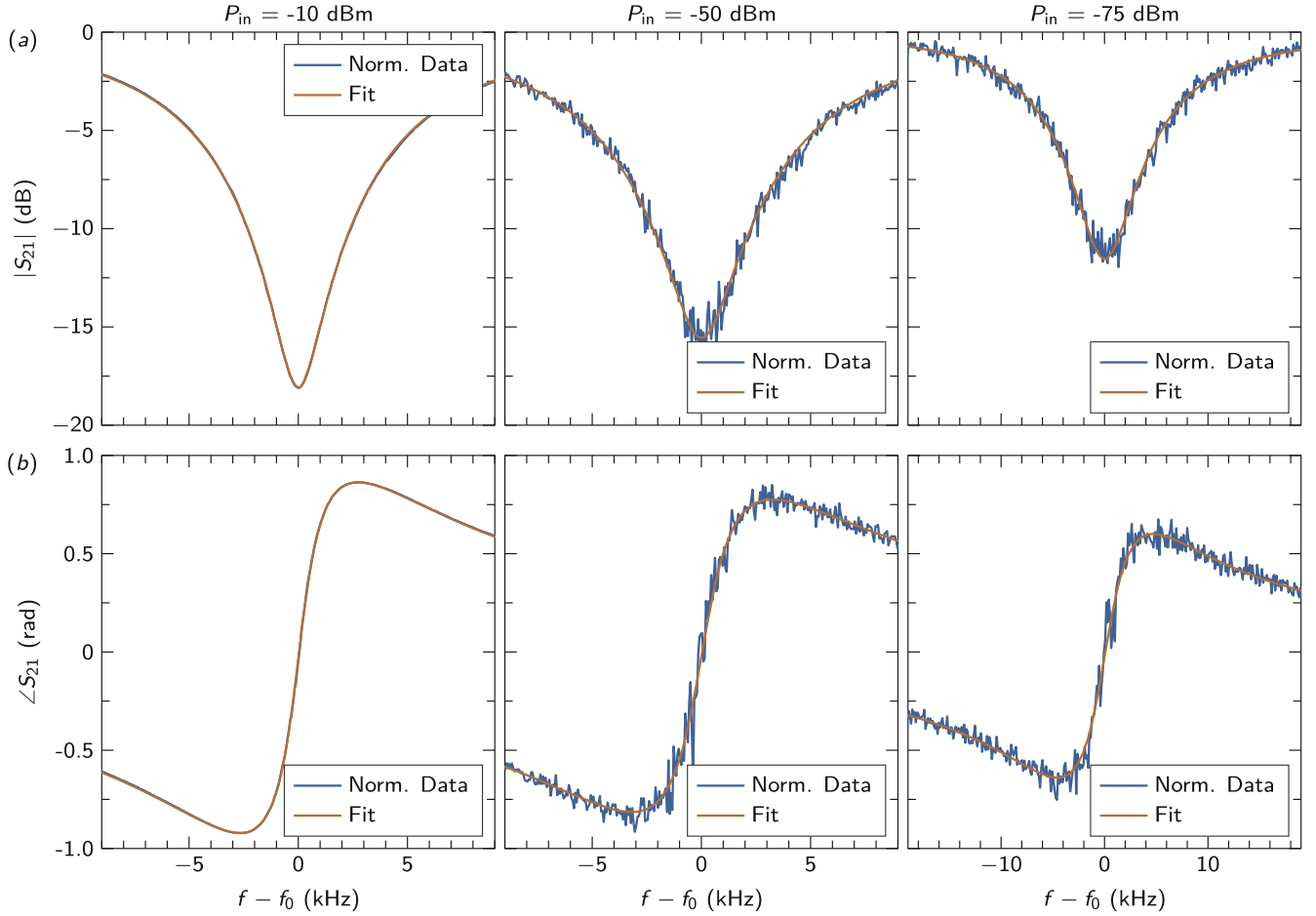
Figure A4. Resonator fitting procedure. Each panel comprises three columns, one for each different excitation power (see appendix text for details). (a) Transmission-coefficient magnitude $|S_{21}|$ versus frequency span $f - f_0$; normalized resonator data ('Norm. Data'; blue (dark gray)) and fitting curves ('Fit'; orange (light gray)). (b) Same as in (a), but for the transmission-coefficient phase $\angle S_{21}$ versus $f - f_0$. The fitting curves are obtained by first inverting the normalized resonator data, fit as explained in the appendix text, re-invert the fitting data, and then plot them over the normalized resonator data.

The resonator measurement procedure comprises the following steps.

(1) Set an approximate value of f_0 and Δf as input values.
(2) Acquire an S_{21} trace centered about the input value f_0 and with span Δf.
(3) Identify the resonator by fitting the data. If the fitting fails, abort; if it succeeds, update the value of f_0 and choose the new frequency span to be $10 \times f_0 / Q_i$.
(4) Perform a loop over the values $\{P_{in}^j\}$:
   (a) set the jth value P_{in}^j and the corresponding Δf_{IF}^j;
   (b) continue the loop as long as the fitting error is above the preset threshold or until N_{tr} is reached:
      (i) acquire a trace and average it with the previously acquired trace for the present value of P_{in}^j;
      (ii) fit the averaged traces.
   (c) If the loop is completed successfully (i.e., the fitting error is below threshold), update f_0 and Δf as before and move to the next excitation power; otherwise abort the procedure.

Figures A3 and A4 show normalization and resonator data as well as fitting curves obtained from the inverse fitting procedure for three different excitation powers, $P_{in} = -10$, -50, and -75 dB mW (dBm), and corresponding IF bandwidths, $\Delta f_{IF} = 300$, 100, and 5 Hz.

Appendix B. COMSOL numerical simulations

The results reported in table 3 of the main text are obtained by modeling the CPW resonators of design 1 and 2 and simulating them with COMSOL Multiphysics. We use a fixed terminal boundary condition with an electrostatic potential of 1 V applied to the CPW center conductor; all other conductors are grounded. The mesh parameters used as input to the COMSOL linear solver, which is based on the LU decomposition, are summarized in table B1. We note that all mesh elements, as well as the number of degrees of freedom solved, for design 2 are two times larger than for design 1. This is to be expected as the cross-sectional surfaces (σ_{i2}) for regions Ω_{i2} in design 2 are approximately two times larger than those (σ_{i1}) for the corresponding regions Ω_{i1} in design 1. It is also worth noting that, for both designs, the minimum element quality is larger than the recommended value of 0.1.

The numerical values of the absolute filling factors for both design 1 and design 2, F_{i1} and F_{i2}, respectively, are also reported in table B1. These values are calculated by

Table B1. Simulation parameters used in the model generated by COMSOL Multiphysics for both design 1 and design 2. We use two-dimensional triangular mesh elements in all simulations. Mesh properties: geometric characteristics of each mesh (number of triangular, edge, and vertex elements) and associated statistics (minimum element quality); additionally, we indicate the number of degrees of freedom solved in each model. Details and definitions on geometric characteristics and statistics are available[1]. Absolute filling factors for design 1 and 2. F_{SM}, F_{SA}, F_{MA}, F_{Si}, and F_0: Absolute filling factors for the SM, SA (vacuum), MA (vacuum), Si, and vacuum regions, respectively. These values are used to find the exact relative filling factors reported in table 3 of the main text. All numerical values are calculated by means of COMSOL Multiphysics (see main and appendix text for details).

Mesh properties	Design 1	Design 2
Triangular elements	536775	1001340
Edge elements	37494	68922
Vertex elements	36	36
Minimum element quality	0.2760	0.2687
Degrees of freedom solved	909057	1739456
Absolute filling factors	Design 1	Design 2
F_{SM}	0.1001	0.0524
F_{SA}	0.0897	0.0462
F_{MA}	0.0091	0.0044
F_{Si}	91.6730	91.8910
F_0	8.1284	8.0064

---

[1] See https://comsol.com/multiphysics/finite-element-method for an introduction to the finite element method and https://comsol.com/blogs/how-to-inspect-your-mesh-in-comsol-multiphysics for details and definitions on geometric characteristics and statistics in COMSOL Multiphysics.

integrating numerically the double integrals in (4a) using COMSOL Multiphysics. The absolute filling factors for the Si and vacuum regions are obtained by changing the index i with j in the numerator of (4a).

ORCID iDs

M Mariantoni ● https://orcid.org/0000-0002-9235-5719

References

[1] Neill C *et al* 2018 *Science* **360** 195–9
[2] Boixo S, Isakov S V, Smelyanskiy V N, Babbush R, Ding N, Jiang Z, Bremner M J, Martinis J M and Neven H 2017 Characterizing quantum supremacy in near-term devices *Nat. Phys.* **14** 595–600
[3] Ladd T D, Jelezko F, Laflamme R, Nakamura Y, Monroe C and O'Brien J L 2010 *Nature* **464** 45–53
[4] Clarke J and Wilhelm F K 2008 *Nature* **453** 1031–42
[5] Wendin G 2017 *Rep. Prog. Phys.* **80** 106001
[6] Gambetta J M, Chow J M and Steffen M 2017 *npj Quantum Inf.* **3** 2
[7] Kelly J *et al* 2015 *Nature* **519** 66–9
[8] Otterbach J S *et al* 2017 Unsupervised machine learning on a hybrid quantum computer (arXiv:1712.05771)
[9] Knight W 2017 MIT Technology Review https://technologyreview.com/s/609451/
[10] Giles M and Knight W 2018 MIT Technology Review https://technologyreview.com/s/610274/
[11] Barends R *et al* 2013 *Phys. Rev. Lett.* **111** 080502
[12] Kamal A, Yoder J L, Yan F, Gudmundsen T J, Hover D, Sears A P, Welander P, Orlando T P, Gustavsson S and Oliver W D 2016 Improved superconducting qubit coherence with high-temperature substrate annealing (arXiv:1606.09262)
[13] Gambetta J M, Murray C E, Fung Y K K, McClure D T, Dial O, Shanks W, Sleight J W and Steffen M 2017 *IEEE Trans. Appl. Supercond.* **27** 1700205
[14] Barends R *et al* 2014 *Nature* **508** 500–3
[15] Jeffrey E *et al* 2014 *Phys. Rev. Lett.* **112** 190504
[16] McKay D C, Sheldon S, Smolin J A, Chow J M and Gambetta J M 2017 Three qubit randomized benchmarking (arXiv:1712.06550)
[17] Martinis J M 2015 *npj Quantum Inf.* **1** 15005
[18] Serniak K, Hays M, de Lange G, Diamond S, Shankar S, Burkhart L D, Frunzio L, Houzet M and Devoret M H 2018 *Phys. Rev. Lett.* **121** 157701
[19] Wisbey D S, Gao J, Vissers M R, da Silva F C S, Kline J S, Vale L and Pappas D P 2010 *J. Appl. Phys.* **108** 093918
[20] Wenner J *et al* 2011 *Appl. Phys. Lett.* **99** 113513
[21] Calusine G *et al* 2018 *Appl. Phys. Lett.* **112** 062601
[22] Anderson P, Halperin B and Varma C 1972 *Phil. Mag.* A **25** 1–9
[23] Phillips W 1981 *Amorphous Solids: Low-Temperature Properties* ed W A Phillips and A C Anderson (Berlin, New York: Springer)
[24] Phillips W A 1987 *Rep. Prog. Phys.* **50** 1657
[25] Martinis J M *et al* 2005 *Phys. Rev. Lett.* **95** 210503
[26] Müller C, Cole J H and Lisenfeld J 2017 Towards understanding two-level-systems in amorphous solids—insights from quantum devices (arXiv:1705.01108)
[27] Gao J, Zmuidzinas J, Mazin B A, LeDuc H G and Day P K 2007 *Appl. Phys. Lett.* **90** 102507
[28] Collin R E 2001 *Foundations for Microwave Engineering* 2nd edn (New York and Hoboken, NJ: IEEE and Wiley)
[29] McRae C R H, Béjanin J H, Earnest C T, McConkey T G, Rinehart J R, Deimert C, Thomas J P, Wasilewski Z R and Mariantoni M 2018 *J. Appl. Phys.* **123** 205304
[30] Nsanzineza I and Plourde B L T 2014 *Phys. Rev. Lett.* **113** 117002
[31] Dunsworth A *et al* 2017 *Appl. Phys. Lett.* **111** 022601
[32] Ofek N *et al* 2016 *Nature* **536** 441–5
[33] O'Connell A D *et al* 2008 *Appl. Phys. Lett.* **92** 112903
[34] Sage J M, Bolkhovsky V, Oliver W D, Turek B and Welander P B 2011 *J. Appl. Phys.* **109** 063915
[35] Martinis J M and Megrant A 2014 UCSB final report for the CSQ program: review of decoherence and materials physics for superconducting qubits (arXiv:1410.5793)
[36] Megrant A *et al* 2012 *Appl. Phys. Lett.* **100** 113510
[37] Bruno A, de Lange G, Asaad S, van der Enden K L, Langford N K and DiCarlo L 2015 *Appl. Phys. Lett.* **106** 182601
[38] Richardson C J K, Siwak N P, Hackley J, Keane Z K, Robinson J E, Arey B, Arslan I and Palmer B S 2016 *Supercond. Sci. Technol.* **29** 064003
[39] Burnett J, Bengtsson A, Niepce D and Bylander J 2018 *J. Phys.: Conf. Ser.* **969** 012131
[40] Kern W 1993 *Handbook of Semiconductor Wafer Cleaning Technology: Science, Technology, and Applications* (*Materials Science and Process Technology Series*) (Norwich, NY: Noyes Publications)
[41] Tournet J, Gosselink D, Miao G X, Jaikissoon M, Langenberg D, McConkey T G, Mariantoni M and Wasilewski Z R 2016 *Supercond. Sci. Technol.* **29** 064004

[42] Béjanin J H *et al* 2016 *Phys. Rev. Appl.* **6** 044010
[43] McRae C R H, Béjanin J H, Pagel Z, Abdallah A O, McConkey T G, Earnest C T, Rinehart J R and Mariantoni M 2017 *Appl. Phys. Lett.* **111** 123501
[44] Mayer J, Giannuzzi L A, Kamino T and Michael J 2007 *MRS Bull.* **32** 400–7
[45] Faoro L and Ioffe L B 2015 *Phys. Rev.* B **91** 014201
[46] Neill C *et al* 2013 *Appl. Phys. Lett.* **103** 072601
[47] Burnett J *et al* 2014 *Nat. Commun.* **5** 4119
[48] Ramanayaka A N, Sarabi B and Osborn K D 2015 Evidence for universal relationship between the measured $1/f$ permittivity noise and loss tangent created by tunneling atoms (arXiv:1507.06043)
[49] Müller C, Lisenfeld J, Shnirman A and Poletto S 2015 *Phys. Rev.* B **92** 035442
[50] Lisenfeld J, Grabovskij G J, Müller C, Cole J H, Weiss G and Ustinov A V 2015 *Nat. Commun.* **6** 6182
[51] Chu Y, Axline C, Wang C, Brecht T, Gao Y Y, Frunzio L and Schoelkopf R J 2016 *Appl. Phys. Lett.* **109** 112601
[52] Morgan S P 1949 *J. Appl. Phys.* **20** 352–62

[53] Hammerstad E O and Bekkadal F 1975 A microstrip handbook *ELAB Report* STF44 A74169 University of Trondheim, Norway
[54] Gross R, Marx A and Deppe F 2016 *Applied Superconductivity: Josephson Effect and Superconducting Electronics* (*De Gruyter Textbook Series*) (Berlin: Walter De Gruyter)
[55] Steinberg K, Scheffler M and Dressel M 2008 *Phys. Rev.* B **77** 214517
[56] Khukhareva I S 1963 *Sov. J. Exp. Theor. Phys.* **16** 828
[57] Wu Z and Davis L E 1994 *J. Appl. Phys.* **76** 3669–72
[58] Quintana C M *et al* 2014 *Appl. Phys. Lett.* **105** 062601
[59] Chiaro B *et al* 2016 *Supercond. Sci. Technol.* **29** 104006
[60] Kwon S *et al* 2018 *J. Appl. Phys.* **124** 033903
[61] Koch R H, DiVincenzo D P and Clarke J 2007 *Phys. Rev. Lett.* **98** 267003
[62] Kumar P, Sendelbach S, Beck M A, Freeland J W, Wang Z, Wang H, Yu C C, Wu R Q, Pappas D P and McDermott R 2016 *Phys. Rev. Appl.* **6** 041001
[63] Grünhaupt L *et al* 2017 *Appl. Phys. Lett.* **111** 072601
[64] Wu X, Long J L, Ku H S, Lake R E, Bal M and Pappas D P 2017 *Appl. Phys. Lett.* **111** 032602